Magnesium-rich crustal compositions on Mercury: Implications for magmatism from petrologic modeling

Karen R. Stockstill-Cahill,[1] Timothy J. McCoy,[1] Larry R. Nittler,[2] Shoshana Z. Weider,[2] and Steven A. Hauck II[3]

Received 25 May 2012; revised 27 September 2012; accepted 25 October 2012; published 22 December 2012.

[1] We have conducted petrologic modeling of MESSENGER-derived compositions and analog compositions to gain a better understanding of the petrogenesis of the crust of Mercury. Analog compositions included a 1425°C partial melt of the Indarch (EH4) meteorite and a range of Mg-rich terrestrial rocks (magnesian basalt, basaltic komatiite, and peridotitic komatiite). All models were held at the iron-wüstite buffer to simulate the reducing conditions that likely existed during Mercury's formation. We then compared modeled mineral compositions and abundances, liquidus temperatures, and viscosities to better constrain the characteristics of the lavas that erupted on Mercury's surface. Our results show that the surface composition of Mercury is most similar to that of a terrestrial magnesian basalt (with lowered FeO), composed mainly of Mg-rich orthopyroxene and plagioclase. Because the model magmas are Mg-rich, their counterparts on Mercury would have erupted at high temperatures and displayed low viscosities. Producing melts of these compositions would have required high temperatures at the mantle source regions on Mercury. The inferred low-viscosity lavas would have erupted as thin, laterally extensive flows (depending upon their effusion rate) and would be expected to display surficial flow features that might be preserved to the present.

Citation: Stockstill-Cahill, K. R., T. J. McCoy, L. R. Nittler, S. Z. Weider, and S. A. Hauck II (2012), Magnesium-rich crustal compositions on Mercury: Implications for magmatism from petrologic modeling, *J. Geophys. Res.*, *117*, E00L15, doi:10.1029/2012JE004140.

1. Introduction

[2] Mercury is a potential compositional end-member in planetary formation and evolution, and thus provides insight into the terrestrial planets as a group [*Chapman*, 1988; *Vilas*, 1988; *Solomon et al.*, 2001]. Despite decades of remote-sensing observations and the Mariner 10 flyby measurements of 1974–75, few constraints had been placed on the surface composition of Mercury prior to the 2004 launch of the MErcury Surface, Space ENvironment, GEochemistry, and Ranging (MESSENGER) spacecraft, and the innermost planet long remained one of the least understood solar system bodies [*Chapman*, 1988; *Solomon et al.*, 2001]. MESSENGER, which flew by Mercury three times in 2008–2009 and was inserted into orbit about Mercury in 2011, carries a suite of instruments optimized to make key measurements regarding the composition and properties of the surface and atmosphere of Mercury [*Solomon et al.*, 2001].

[3] The X-Ray Spectrometer (XRS) and Gamma-Ray Spectrometer (GRS) measurements obtained by MESSENGER since orbit insertion have greatly improved our knowledge of the composition of the surface of Mercury. XRS spectra indicate that the surface, normalized to the Si abundance, has relatively high abundances of Mg and S, but is low in Al and Ca and very low in Fe, Ti, Cl, Cr, and Mn [*Nittler et al.*, 2011] compared with typical terrestrial and lunar crustal materials. GRS spectra indicate an average K/Th ratio on the surface of Mercury (northward of ~20°S) that is comparable to those for the other terrestrial planets and an order of magnitude higher than lunar values, although the absolute abundances of K and Th are 3–4 times lower than on the surface of Mars [*Peplowski et al.*, 2011].

[4] We have conducted petrologic modeling of Mercury crustal compositions, derived from MESSENGER data and analog compositions (Table 1), using the MELTS program [*Ghiorso and Sack*, 1995; *Asimov and Ghiorso*, 1998]. Although the MELTS program has limitations when applied to compositions and pressure (P), temperature (T), and oxygen fugacity (fO_2) conditions that differ strongly from the terrestrial norm [e.g., *Slater et al.*, 2003; *Thompson et al.*, 2003], petrologic modeling is a more flexible approach than conducting relevant experiments, particularly given that

[1]Department of Mineral Sciences, National Museum of Natural History, Smithsonian Institution, Washington, D. C., USA.
[2]Department of Terrestrial Magnetism, Carnegie Institution of Washington, Washington, D. C., USA.
[3]Department of Earth, Environmental, and Planetary Sciences, Case Western Reserve University, Cleveland, Ohio, USA.

Corresponding author: K. R. Stockstill-Cahill, Department of Mineral Sciences, National Museum of Natural History, Smithsonian Institution, Washington, DC 20013, USA. (cahillk@si.edu)

0148-0227/12/2012JE004140

Table 1. Measured and Possible Analog Compositions (wt % Oxide/Element) for Mercury Surface Material

	NVP[a]	IcP-HCT[a]	Indarch Melt, 1425°C[b]	Magnesian Basalt[c]	Basaltic Komatiite[c]	Peridotitic Komatiite[c]
SiO_2	57.0	52.4	52.7	52.2	50.4	42.8
TiO_2	0.89[d]	0.82[d]	0.21	0.59	0.65	0.22
Al_2O_3	14.9	12.2	13.5	12.3	11.3	4.52
Cr_2O_3	0.77[d]	0.70[d]	b.d.	-	-	-
FeO	3.43[d]	3.15[d]	0.25	11.6	9.91	11.5
MnO	0.69[d]	0.63[d]	0.12	0.18	0.19	0.24
MgO	16.0	22.1	19.1	10.6	14.4	33.6
CaO	4.69	5.99	11.7	11.5	10.5	5.73
Na_2O	0.23[e]	0.11[e]	b.d.	0.58	2.34	0.29
K_2O	0.21	0.10	b.d.	0.29	0.00	0.04
S	1.23	1.78	4.36	-	-	-
Total	100.00	100.00	101.94	99.84	99.69	98.94
Al/Si	0.296	0.264	0.290	0.267	0.254	0.120
Mg/Si	0.361	0.545	0.468	0.262	0.369	1.013
Ca/Si	0.126	0.175	0.339	0.337	0.319	0.205

[a]From *Weider et al.* [2012], unless otherwise noted.
[b]From *McCoy et al.* [1999]; b.d. denotes an abundance below detection.
[c]From *Basaltic Volcanism Study Project* [1981].
[d]FeO and TiO_2 were calculated from global average data of *Nittler et al.* [2011], and Cr_2O_3 and MnO were calculated from upper limits given by *Nittler et al.* [2011].
[e]Notwithstanding the determination of the Na abundance in Mercury surface material [*Evans et al.*, 2012], the Na abundance was initially set equal to that of K (see text) derived from MESSENGER GRS data by *Peplowski et al.* [2011].

MESSENGER-derived compositions are still being revised and refined. Modeling is a logical prelude to experimental studies that can be executed once the orbital data converge to one or more final compositions. The objective of the modeling is to improve our understanding of the properties of magmas on Mercury (e.g., viscosity, temperature), their likely crystallizing mineralogies, and, through comparison with analogs, crustal petrogenesis more generally.

2. Methods

2.1. MELTS Crystallization Modeling

[5] Equilibrium crystallization models were examined with the MELTS software [*Ghiorso and Sack*, 1995; *Asimov and Ghiorso*, 1998] for the measured and candidate analog compositions given in Table 1. From the high bulk density and low surface FeO content of Mercury, early magmatic conditions on Mercury are thought to have included strongly reducing conditions, i.e., values of oxygen fugacity (fO_2) 3 to 6.5 $\log_{10}$ units below the iron-wüstite (IW) buffer [*Malavergne et al.*, 2010; *Zolotov*, 2011]. However, this inferred fO_2 may be biased low if surface FeO has been reduced to Fe by ion sputtering and micrometeoroid bombardment [*Malavergne et al.*, 2010]. More recent estimates of the oxygen fugacity of Mercury, derived from MESSENGER XRS surface measurements of both S and Fe, show good agreement with previous values and range from 2.6 to 6.3 $\log_{10}$ units below the IW buffer [*McCubbin et al.*, 2012].

[6] MELTS has been shown to produce poor matches to the mineralogy of meteorites and lunar basalts at lower oxygen fugacities [*Slater et al.*, 2003; *Thompson et al.*, 2003], presumably because the code is better calibrated for terrestrial (i.e., more oxidizing) conditions. We ran MELTS for a range of highly reducing conditions, which revealed that oxygen fugacities below IW did not markedly change the resulting rock and mineral compositions. The models in this paper were therefore held at the IW buffer during crystallization modeling. Modeling began 20°C above the liquidus temperature (T_{liq}) as calculated by MELTS for a given composition, tracked temperature in 20°C steps, and was carried to a final temperature ~400 to 500°C below the liquidus temperature to approximate the solidus. However, MELTS halted at a higher temperature if the solidus was reached or if a key component (i.e., a major oxide) was exhausted. Pressure was held at 1 bar throughout the crystallization modeling. The resulting mineral and rock compositions were compared among the models. Magma viscosities at liquidus temperatures were calculated from these same compositions following the method of *Shaw* [1972].

2.2. Modeled Starting Magma Compositions

[7] Modeled Mercury crustal compositions include that for the northern volcanic plains (NVP) and that for the older surrounding intercrater plains and heavily cratered terrain (IcP-HCT), both derived from an early iteration of the XRS data presented by *Weider et al.* [2012] and from GRS data from *Peplowski et al.* [2011]. The NVP is a large contiguous area of smooth plains that cover much of Mercury's high northern latitudes and have been interpreted as products of flood lavas that erupted shortly after the end of the late heavy impact bombardment of the inner solar system [*Head et al.*, 2011]. The IcP-HCT is stratigraphically older and displays a generally higher density of impact craters than smooth plains deposits [*Spudis and Guest*, 1988].

[8] Analog compositions include the 1425°C partial melt of the Indarch (EH4) meteorite [*McCoy et al.*, 1999] and Mg-rich terrestrial rocks. The Indarch melt composition corresponds to ~29% partial melting of the bulk meteorite and contains ~4 wt % S [*McCoy et al.*, 1999], so the melt would be expected to contain ~6 vol % sulfides [*Burbine et al.*, 2002]. The Mg-rich terrestrial rocks include a magnesian basalt, a basaltic komatiite, and a peridotitic komatiite [*Basaltic Volcanism Study Project*, 1981]. The measured and analog compositions are listed in Table 1 and plotted in Figure 1. For the purposes of this study, we distinguished

these rock types in the manner defined by the *Basaltic Volcanism Study Project* [1981], i.e., magnesian basalts contain 8.5–12 wt % MgO, basaltic komatiites contain 12–20 wt % MgO, and peridotitic komatiites contain >20 wt % MgO. It should also be noted that these compositions are distinguishable in terms of the International Union of Geological Sciences (IUGS) total-alkali silica (TAS) classification, with the magnesian basalt and basaltic komatiite plotting within the basalt field (hence requiring the term "basalt" as their name or modifier) and the peridotitic komatiite plotting within the picrobasalt field.

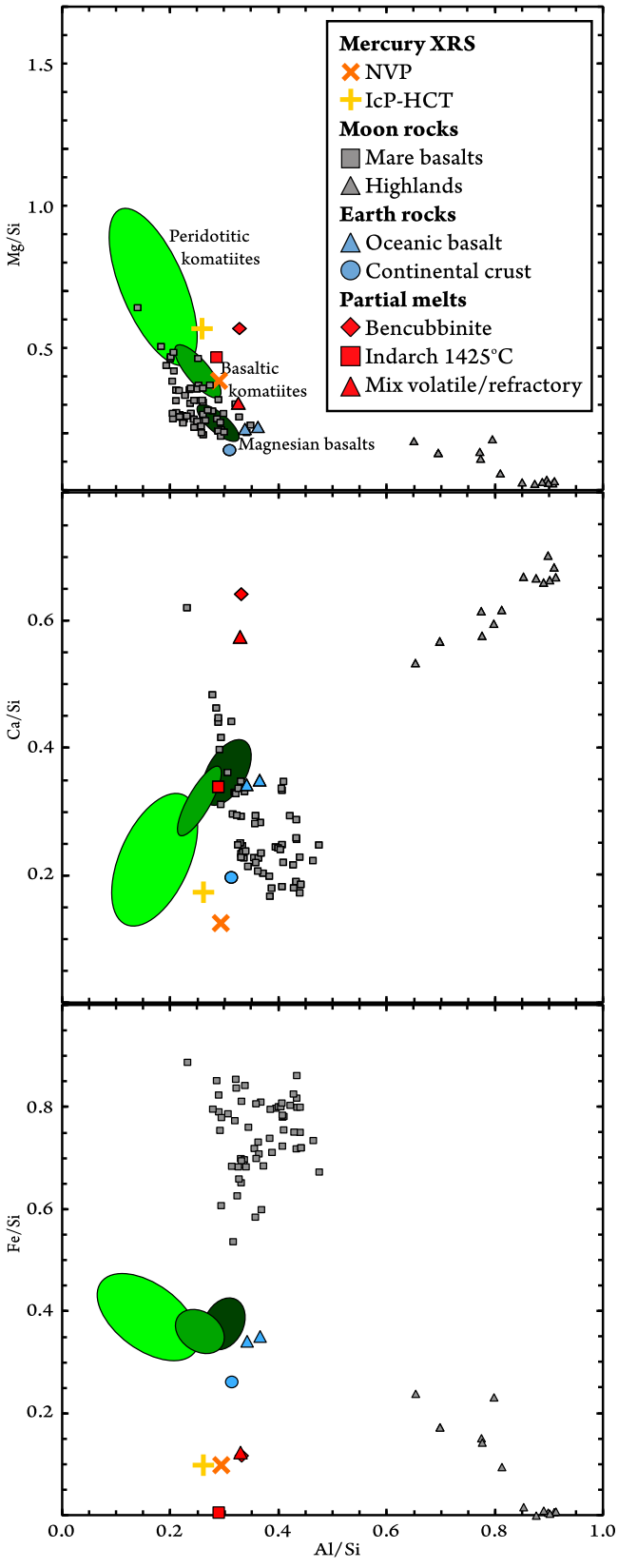

[9] Elemental ratios derived from the average XRS spectra for the NVP and the IcP-HCT areas were adopted as MESSENGER-based compositions for the surface of Mercury. The ratios include Mg/Si, Al/Si, Ca/Si, S/Si, Ti/Si, and Fe/Si. To derive elemental abundances from elemental ratios, the ratios were multiplied by ~25 wt % Si [after *Nittler et al.*, 2011] and the total was renormalized. Elemental abundances were converted to oxide abundances and renormalized. In addition, we set abundances equal to the upper limits for Cr and Mn, both 0.5 wt %, derived from XRS data [*Nittler et al.*, 2011] and K abundances calculated from GRS data [*Peplowski et al.*, 2011].

[10] In terrestrial Mg-rich volcanic and continental crustal rocks, the Na abundance is generally comparable to the K abundance. Initially, in the absence of other abundance data for Na, the Na abundances were set equal to the K abundances for modeling the measured surface compositions. *Evans et al.* [2012] have reported a global average Na abundance, based on GRS measurements, of ~3 wt %, suggesting an order of magnitude greater Na abundance than that of K. The source of the Na and its variability across the surface of Mercury are not known at this point, raising the possibility that the measurement might reflect a late veneer distributed inhomogeneously across the planet rather than a primary characteristic of the igneous rocks erupted on the surface of Mercury. If Na were added as a late veneer, Na would be coupled with other volatiles, particularly K and S. However, K abundances are relatively low and therefore do not strongly influence the model results. Sulfur, although more abundant, doesn't markedly influence the proportion of major phases (plagioclase, mafic silicates) that crystallize. In fact, the major influence on the relative proportion of major phases is the abundance of Si and Al. Since albite ($NaAlSi_3O_8$) includes more Si and less Al than anorthite ($CaAl_2Si_2O_8$), the effect of higher Na abundance is to produce a higher abundance of plagioclase that has a higher albite content and favor the crystallization of relatively Si-poor olivine ($(Mg, Fe)_2SiO_4$) over orthopyroxene

Figure 1. Elemental ratios for areas on Mercury, derived from MESSENGER XRS observations, are compared with those for Mg-rich terrestrial rocks (green fields), lunar rocks (gray symbols [*Papike et al.*, 1998]), terrestrial crustal rocks (blue symbols [*Lodders and Fegley*, 1998]), and partial melts of a bencubbinite chondrite [*Taylor and Scott*, 2003], the enstatite chondrite Indarch [*McCoy et al.*, 1999], and a mix of refractory and volatile materials (red symbols [*Morgan and Anders*, 1980]). The fields for terrestrial peridotitic komatiites, basaltic komatiites, and magnesian basalts, shown in green, represent ranges of compositions reported by the *Basaltic Volcanism Study Project* [1981] and the Geochemical Rock Database (http://georoc.mpch-mainz.gwdg.de/georoc/Entry.html accessed on 15 December 2011). Figure modified from *Nittler et al.* [2011].

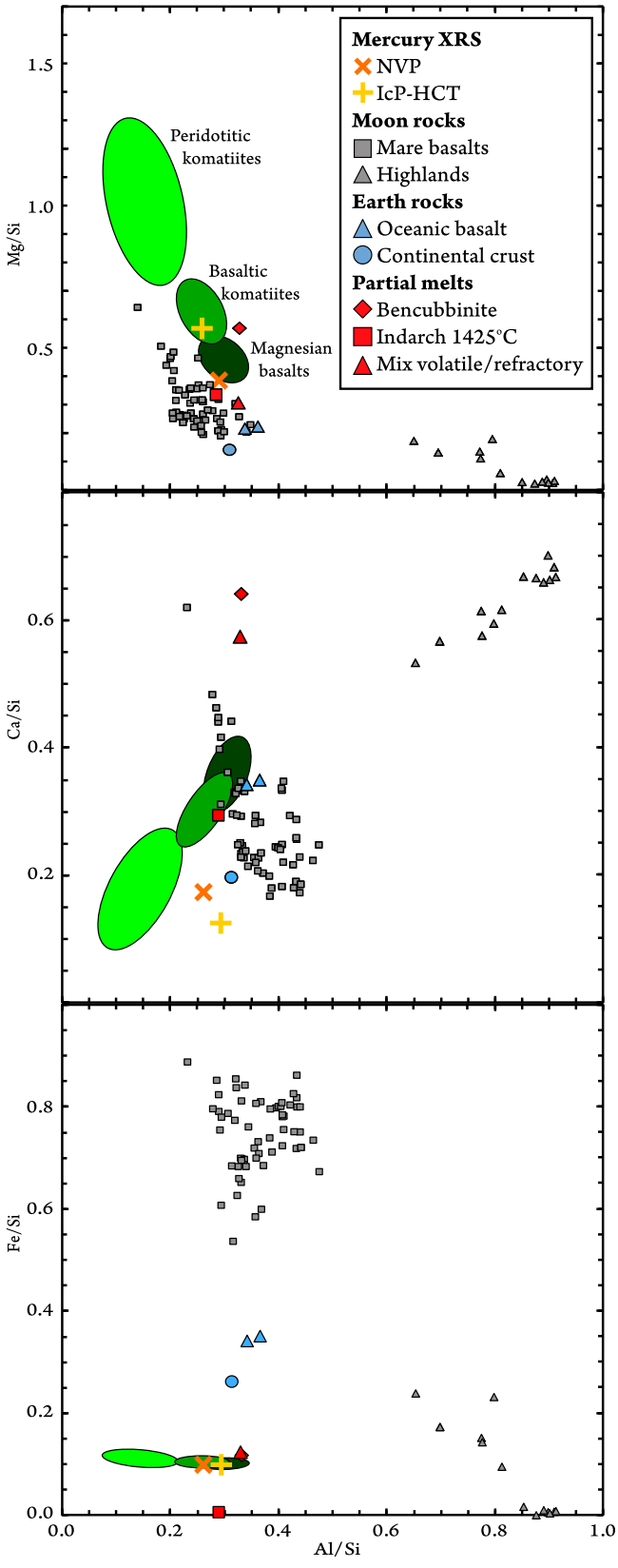

Figure 2. Elemental ratios for Mercury, as in Figure 1, but with Fe decreased for the Mg-rich terrestrial rocks and S removed for S-rich compositions (see text). Symbols have the same meaning as those in Figure 1.

((Ca, Mg, Fe)$_2$Si$_2$O$_6$). For this reason, we first present our results with Na abundances set equal to the K abundances, and we then compare the results to those for which the higher global average Na abundance is adopted.

[11] Several modifications to these compositions were made prior to crystallization modeling to account for differences in FeO contents between terrestrial analog and Mercury compositions as well as the challenges to the MELTS software posed by large S contents. First, we modified the FeO contents of the terrestrial analogs. The FeO contents of the terrestrial Mg-rich rocks are much higher than the limit of 2–5 wt % FeO for the surface of Mercury [*Sprague et al.*, 2009; *Nittler et al.*, 2011] (Table 1). Magmas of these compositions would crystallize silicates with sufficient FeO to produce a ~1-μm absorption feature in reflectance spectra, not seen in spectral observations of Mercury's surface [e.g., *Vilas*, 1988; *Robinson and Taylor*, 2001; *Blewett et al.*, 2002; *Denevi and Robinson*, 2008; *McClintock et al.*, 2008; *Blewett et al.*, 2009; *Riner et al.*, 2010]. Therefore, the FeO contents of these rocks were decreased to 3 wt % by replacing molar FeO with MgO and renormalizing the totals to emulate expected Mercury magmas. These modified compositions are displayed in Figure 2. Although their MgO contents were raised above 20% by this adjustment, we did not reclassify the magnesian basalt and basaltic komatiite because they did not change fields on the TAS diagram. For clarity, we refer to these modified compositions as "Mg-adjusted." Mg-adjusted compositions of the terrestrial Mg-rich rocks shift to higher Mg/Si and lower Fe/Si after this modification (compare Figures 1 and 2).

[12] The MELTS [*Ghiorso and Sack*, 1995; *Asimov and Ghiorso*, 1998] crystallization calculations are not well-calibrated for sulfur-rich compositions and hence did not run to completion (i.e., the model still had >20% magma remaining; ideally, a final rock composition would have less than ~15%) for the Mercury and Indarch compositions shown in Table 1. It is anticipated that S would form sulfides with Mg and Ca [*Burbine et al.*, 2002; *Nittler et al.*, 2011; *Weider et al.*, 2012]. Therefore, the S present in these compositions was reduced to zero, and equal mole fractions of Mg and Ca were removed to form sulfides and renormalized to 100% prior to MELTS calculations. We used two methods to estimate the ratio of MgS to CaS. First, XRS elemental ratios of Ca/Si and Mg/Si were plotted against S/Si [*Nittler et al.*, 2011], and linear trend lines were calculated. The best fit trends for Mg and Ca were obtained individually and then recast as Mg/(Mg + Ca), yielding the result that sulfides at the surface of Mercury would be ~$Mg_{0.74}Ca_{0.26}S$, under the assumption that the observed Mg and Ca correlations with S result from admixtures of sulfides. Second, scanning electron microscope measurements of 12 miscible sulfides present in the 1425°C Indarch meteorite melt charge of *McCoy et al.* [1999] suggested an average sulfide composition of ~$Mg_{0.79}Ca_{0.21}S$. We note that these sulfides also contained Fe, Cr, and Mn cations. However, these cations were not included in our calculations because (i) MESSENGER-derived data for these cations are upper limits, so the actual amount available to form sulfides is uncertain; (ii) the distribution of these cations in low-Fe, highly reduced systems (such as Indarch) is not fully characterized and their variation

Table 2. Modeled Compositions (wt % Oxide/Element)

	NVP[a]	IcP-HCT[a]	Indarch Melt, 1425°C[a]	Magnesian Basalt[b]	Basaltic Komatiite[b]	Peridotitic Komatiite[b]
SiO_2	58.9	54.9	59.3	50.9	49.4	41.8
TiO_2	0.92	0.86	0.24	0.58	0.64	0.21
Al_2O_3	15.4	12.8	15.2	12.0	11.1	4.41
Cr_2O_3	0.79	0.74	0.00	-	0.00	0.00
FeO	3.54	3.30	0.28	3.00	3.00	3.00
MnO	0.71	0.66	0.13	0.18	0.19	0.23
MgO	14.9	20.9	15.4	21.1	22.8	43.4
CaO	4.40	5.63	11.4	11.2	10.3	5.59
Na_2O	0.24	0.12	0.00	0.57	2.29	0.28
K_2O	0.21	0.10	0.00	0.28	0.00	0.04
S	0.00	0.00	0.00	-	-	-
Total	100.00	100.00	101.94	99.84	99.69	98.94
T_{Liq} (°C)[c]	1512	1537	1381	1453	1571	1680
η (Pa·s)[d]	5.9	1.05	14.2	0.83	0.25	0.02
Al/Si	0.296	0.264	0.290	0.267	0.254	0.120
Mg/Si	0.327	0.491	0.335	0.534	0.595	1.340
Ca/Si	0.114	0.157	0.295	0.337	0.319	0.205

[a]Sulfur-free compositions as described in the text.
[b]Mg-adjusted compositions as described in the text.
[c]Liquidus temperature calculated by MELTS.
[d]Viscosity derived following *Shaw* [1972].

not fully understood; and (iii) the effect of removing these cations did not result in sufficiently large changes to the abundances of sulfide cations (Mg, Ca, Fe, Cr, Mn) to exceed the variation in the MESSENGER-derived compositional data. Therefore, we reduced the Mg and Ca mole for mole with S with a Mg/(Mg + Ca) ratio of 0.75. On the basis of the amount of S removed for these compositions, sulfide abundances of ~2 wt % for the NVP, ~3 wt % for the IcP-HCT, and ~8 wt % for Indarch would be indicated. The compositions resulting from this procedure for S removal are shown in Table 2 and Figure 2. These changes slightly decrease the Mg/Si and Ca/Si ratios for the Mercury and Indarch melt compositions (compare Figures 1 and 2).

2.3. Derivation of X-Ray Spectra for the Model Results

[13] In order to directly compare the analogs with the measured Mercury surface compositions, we produced synthetic XRS spectra for the Indarch 1425°C partial melt and the Mg-adjusted terrestrial analog compositions. The MESSENGER XRS measures fluorescent X-rays (at energies up to ~10 keV) from the top layers (tens of micrometers) of Mercury's regolith that are excited by X-rays emitted from the 10^6 K plasma in the Sun's corona during solar flares [*Schlemm et al.*, 2007]. Observed XRS spectra include both fluorescent lines from the planet and scattered solar X-rays. The fluorescent spectral characteristics depend strongly on the composition of the irradiated material and on the incident solar spectrum. The incident solar flux, however, varies strongly with wavelength, and its intensity changes on timescales of minutes to hours. For this simulation, we used the CHIANTI 6.0 code [*Dere et al.*, 1997; *Landi et al.*, 2006] to calculate synthetic isothermal solar spectra at the two temperatures (8.6 MK and 14.6 MK) at which the two XRS spectra were obtained (see section 3.3). For each solar spectrum and analog composition, the X-ray fluorescence and coherently scattered spectra were calculated for the same conditions as for the original modeling of the flare data, following the methodology of *Clark and Trombka* [1997] and *Nittler et al.* [2001, 2011].

3. Results

3.1. MELTS Modeling: Mineral Abundances and Compositions

[14] Petrologic modeling allows us to understand the expected mineralogy and mineral compositions produced by crystallization of melts of the measured Mercury surface compositions and compare those derived mineral abundances and compositions to those of the Indarch 1425°C melt and Mg-adjusted terrestrial analogs. Modeled rock compositions are illustrated in Figure 3. The modeled Mercury compositions are dominated by orthopyroxene and plagioclase, and as such are classified as norites. Both Mercury compositions are quartz-normative, having 8–22% quartz and smaller amounts of olivine, spinel, and corundum. The crystallization of spinel and corundum may not be a robust finding, since it may be caused by uncertainties in the petrologic models and the measured Mercury compositions. Among the analog compositions, the Mg-adjusted peridotitic komatiites and basaltic komatiites are enriched in olivine relative to the derived Mercury mineralogies; the Indarch 1425°C melt and the Mg-adjusted magnesian basalt contain <10% olivine (Figure 3a). When the pyroxene end-members are distinguished, the derived Mercury mineralogies do not contain clinopyroxene, whereas the Mg-adjusted magnesian basalt contains subequal amounts of orthopyroxene and clinopyroxene, and the Indarch 1425°C melt contains substantial clinopyroxene (Figure 3b). The lack of clinopyroxene in the derived Mercury mineralogies reflects the low Ca abundance measured for Mercury surface material [*Nittler et al.*, 2011] relative to Mg-adjusted terrestrial analogs and the Indarch 1425°C melt compositions (Table 2). We note that recent GRS measurements of Mercury may indicate a somewhat higher global average Ca/Si ratio [*Evans et al.*,

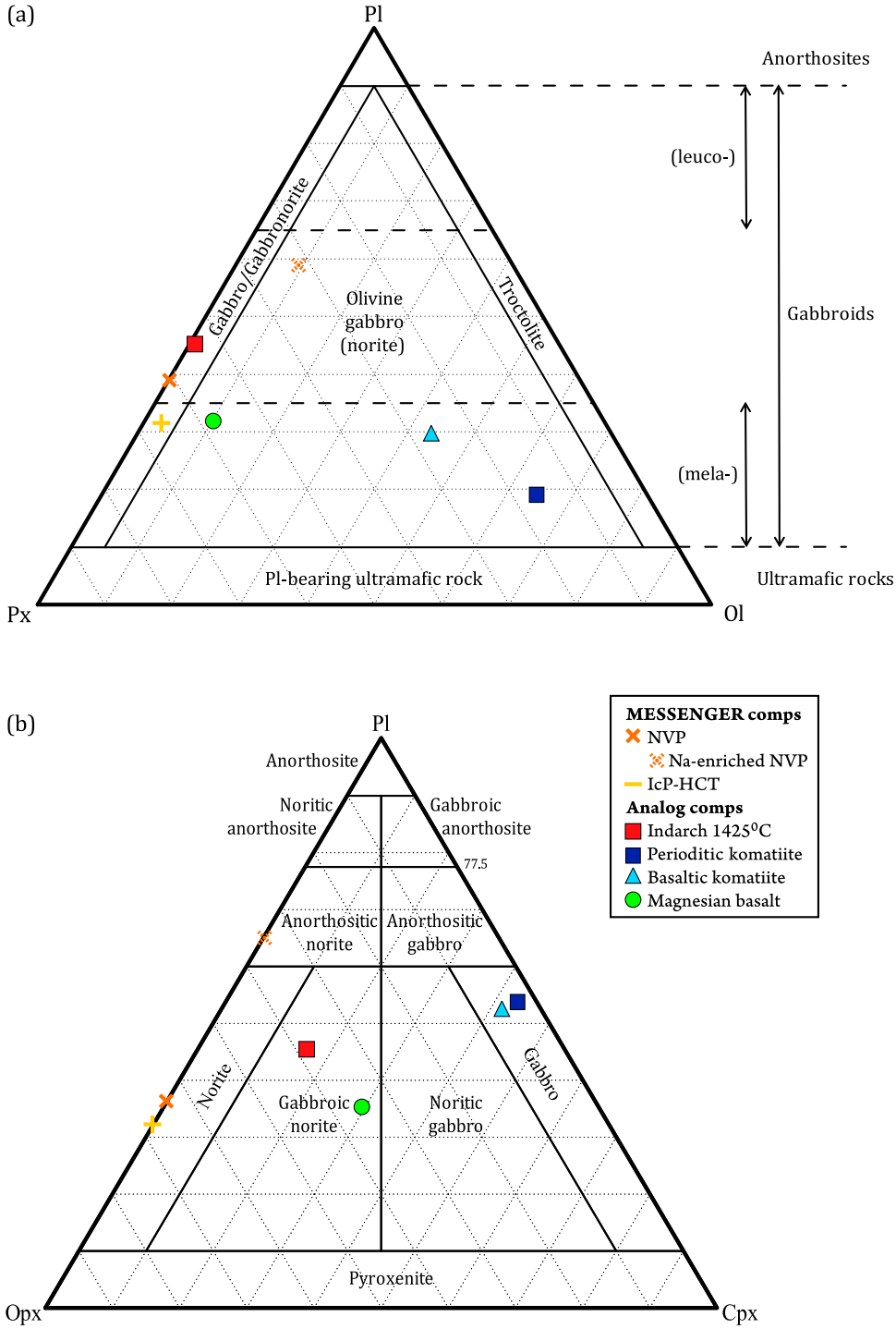

Figure 3. Rock compositions predicted from crystallization modeling of measured and candidate analog compositions plotted on standard rock classification diagrams. (a) Plagioclase–pyroxene–olivine (Pl–Px–Ol) ternary diagram. (b) Plagioclase–orthopyroxene–clinopyroxene (Pl–Opx–Cpx) ternary diagram. Derived from modeled compositions that are S-free (NVP, IcP-HCT, Indarch 1425°C) or Mg-adjusted (magnesian basalt, basaltic komatiite, peridotitic komatiite), as described in the text. The Na-rich NVP rock composition is derived from preliminary modeling using the global average Na abundance as described in the text.

2012], which may indicate that high-Ca clinopyroxene is found elsewhere on the surface of Mercury.

[15] Modeled mineral compositions are listed in Table 3 and displayed in Figure 4. The measured Mercury surface compositions crystallize Mg-rich olivine and orthopyroxene, with the modest FeO concentrations yielding olivine of $Fa_{5–8}$ and orthopyroxene of $Fs_{7–15}$. Plagioclase is calcic, although we discuss the implications of the assumed bulk

Table 3. Crystallization Modeling Results at the Last Temperature Step for Each Composition[a]

Component	NVP (wt %)	IcP-HCT (wt %)	Indarch Melt, 1425°C (wt %)	Magnesian Basalt (wt %)	Basaltic Momatiite (wt %)	Peridotitic Komatiite (wt %)
Sulfides[b]	2	3	8	-	-	-
Liquid	5	2	0	0	3	0
Olivine	2	2	0	11	40	60
	Fa_{8}	$Fa_{5–8}$	$Fa_{1–2}$	$Fa_{4–8}$	$Fa_{3–6}$	$Fa_{2–4}$
Opx	41	58	37	32 $Wo_{2–4}En_{89–91}Fs_{7}$	9	7
	$Wo_{0–1}En_{87–93}Fs_{7–15}$	$Wo_{1–2}En_{91–94}Fs_{6–8}$	$Wo_{1–3}En_{96–98}Fs_{1}$		$Wo_{3}En_{91–92}Fs_{6}$	$Wo_{0–2}En_{94–95}Fs_{4–5}$
Cpx	-	-	18	27 $Wo_{38–46}En_{51–57}Fs_{4–5}$	21	14
			$Wo_{42–47}En_{53–57}Fs_{1}$		$Wo_{41–43}En_{54–56}Fs_{3}$	$Wo_{7–45}En_{53–88}Fs_{2–5}$
Pl	24	28	36	31 $An_{80–88}Or_{0–4}$	27	18
	$An_{83–90}Or_{0–1}$	$An_{94–96}Or_{0–1}$	An_{100} Or_{0}		$An_{64–78}Or_{0–1}$	$An_{83–89}Or_{0–3}$
Spinel	5	1	-	-	-	-
	$C_{18–57}U_{0–2}S_{42–82}$	$C_{28–49}U_{0–2}S_{51–71}$				
Quartz (polymorph)	22	8	-	-	-	-
Corundum	1	-	-	-	-	-

[a]Final component abundances are rounded to the 1% level; dashes indicate components that did not appear in the crystallization model.
[b]Sulfide amount removed prior to MELTS modeling. Mineral compositions represent the range displayed during modeled crystallization and are also shown in Figure 2. Olivine compositions are denoted in terms of the fayalite (Fa) proportion. Orthopyroxene (Opx) and clinopyroxene (Cpx) compositions are denoted in terms of the wollastonite (Wo), enstatite (En), and ferrosilite (Fs) proportions. Plagioclase (Pl) compositions are denoted by the anorthite (An) and orthoclase (Or) proportions. Spinel compositions are denoted by their chromite (C), ulvöspinel (U), and spinel (S) proportions.

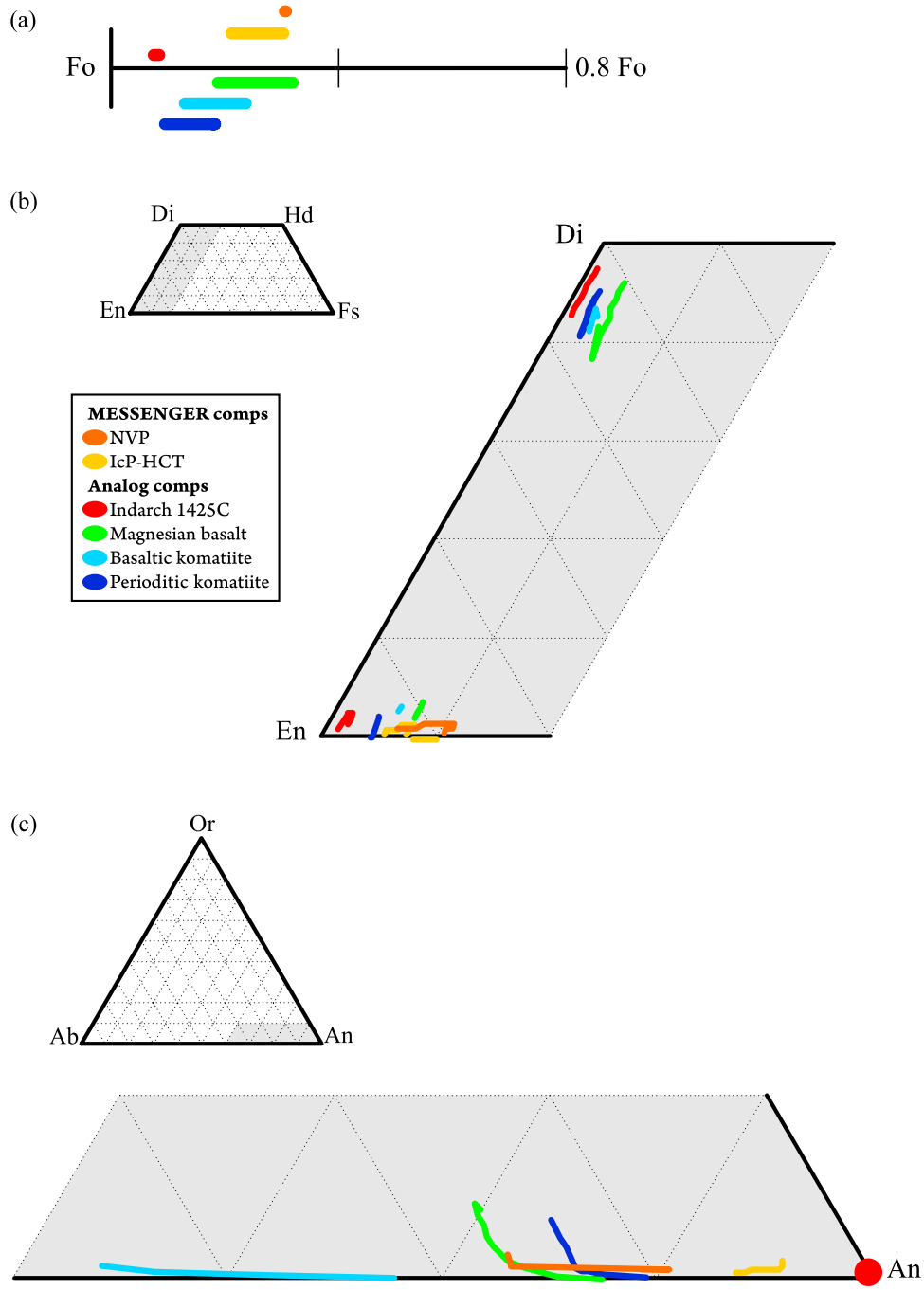

Figure 4. Mineral compositions predicted from crystallization modeling of Mercury and possible candidate compositions for (a) olivine (Fo = forsterite, Fa = fayalite), (b) pyroxenes (Di = diopside, Hd = hedenbergite, En = enstatite, Fs = ferrosilite), and (c) feldspars (Ab = albite, An = anorthite, Or = orthoclase). The Mg-rich portion of the full pyroxene quadrilateral is shown as an inset in Figure 4b. The anorthitic (calcium-rich) corner of the feldspar ternary is shown as an inset in Figure 4c. Derived from modeled compositions that are S-free (NVP, IcP-HCT, Indarch 1425°C) or Mg-adjusted (magnesian basalt, basaltic komatiite, peridotitic komatiite), as described in the text.

sodium concentration on plagioclase compositions below. To first order, the derived mineral compositions among the analogs only moderately match the modeled mineralogies for measured Mercury surface compositions, although some discrimination can be made. The modeled Mercury olivine compositions match best to magnesian basalt (Table 3 and Figure 4a). Although the olivine compositions of the peridotitic komatiite and Indarch partial melt overlap with the Fe-rich end of the basaltic komatiite olivine, they are more Fe-poor than those derived from the Mercury compositions.

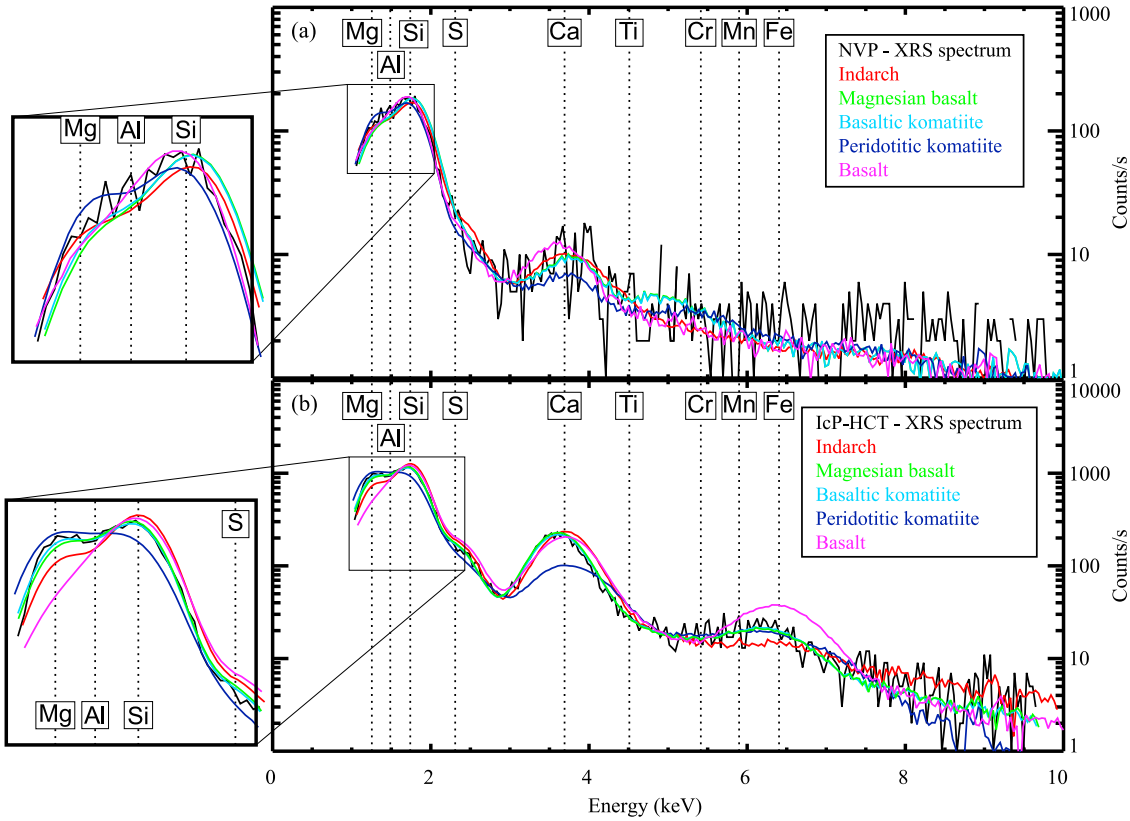

Figure 5. Example XRS spectra for (a) the NVP and for (b) the older IcP-HCT terrain on Mercury, compared with synthetic spectra derived for candidate analog compositions. Synthetic spectra were generated for solar flare temperatures of (a) 8.6 MK and (b) 14.6 MK, the maximum temperatures of the solar flares that produced the XRS spectra (flare 2 and 5, respectively, of *Nittler et al.* [2011]). Insets show the portions of the spectra near the Mg, Al, and Si peaks in greater detail. Derived from modeled compositions that are S-free (NVP, IcP-HCT, Indarch 1425°C) or Mg-adjusted (magnesian basalt, basaltic komatiite, peridotitic komatiite), as described in the text.

An upper limit to Fe/Si in the starting Mercury compositions was used, and thus the olivine modeled for the Mercury compositions likely provides an upper limit on Fe content. The modeled Mercury orthopyroxene compositions just overlap the values derived for magnesian basalts and basaltic komatiites, whereas the Indarch 1425°C melt and peridotitic komatiite produce more magnesian compositions (Figure 4b). The modeled Mercury plagioclase compositions overlap with those of the magnesian basalt and the peridotitic komatiite, but we do not emphasize these matches because there are uncertainties in the Mercury Na abundances that should be included in the models. It is possible that the plagioclase compositions differ from those calculated here, although a higher bulk Na_2O value might not produce more albitic plagioclase compositions. As an example, the basaltic komatiite has an order of magnitude more Na_2O than the other models (Tables 1 and 2) yet has plagioclase compositions that are still dominantly anorthitic and only moderately more Na-rich than other models (Table 3 and Figure 4c).

[16] Modeling of the NVP composition with the higher global average Na abundance of 3 wt % [*Evans et al.*, 2012] indicates differences from the NVP model results presented in Table 3. The most substantial differences obtained with the higher Na abundance are a marked increase in the plagioclase abundance to 57% in the Na-rich composition from 24% in the Na-poor composition and a decrease in the quartz abundance to 0% in the Na-rich composition from 22% in the Na-poor composition. Although the overall mafic silicate abundance remains constant (38% for the Na-rich composition versus 43% for the Na-poor composition), there is a shift in the ratio of orthopyroxene to olivine (30%:8% for the Na-rich composition versus 41%:2% for the Na-poor composition). This shift reflects the greater silica content of albite than anorthite, which would favor the crystallization of relatively Si-poor olivine over orthopyroxene. In terms of composition, the plagioclase exhibits a wider range of compositions ($An_{36–83}$) than previously modeled, but both the average (An_{65}) and final (An_{83}) compositions remain dominantly anorthitic. Interestingly, the final plagioclase compositions in both models are identical (An_{83}). Compositions of orthopyroxene and olivine are similar ($Wo_{2–3}En_{87–90}Fs_{9–10}$ and Fa_8, respectively). In summary, the major changes in model results when the Na abundance is increased to the level measured as a global average (3 wt %) are (i) a large increase

in plagioclase abundance, (ii) a decrease in quartz abundance, (iii) a decrease in the ratio of orthopyroxene to olivine, and (iv) a decrease in the average An content in the model plagioclase composition. Doubling the plagioclase abundance changes the nature of the crust, from a gabbronorite to an olivine gabbronorite in terms of the plagioclase–pyroxene–olivine ternary classification (Figure 3a) and from a norite to an anorthositic norite in terms of the plagioclase–olivine–clinopyroxene ternary classification (Figure 3b). In addition, doubling the plagioclase abundance would increase the albedo of the surface. Such a high albedo runs counter to the generally low albedo of the surface of Mercury, but the effects of a greater plagioclase abundance might be mitigated by the effects of thermal cycling or space weathering. Once Na abundance maps are available, region-specific Na abundances for the NVP and IcP-HCT should be incorporated into modeling to refine and improve the models of the type presented here.

3.2. Liquidus Temperatures and Calculated Viscosities

[17] In addition to modeling crystallization, the MELTS program calculates the temperature of the melt at the liquidus. The MELTS liquidus temperatures for the models range from 1381°C to 1680°C (Table 2). The derived liquidus temperature of 1381°C for the Indarch melt, which formed at the known experimental temperature of 1425°C, yields some confidence that the reasonably high temperatures calculated here are correct, probably with an uncertainty of about ±50°C. Among the analog compositions, the Indarch melt composition has the lowest liquidus temperature. The liquidus temperatures of the Mg-adjusted terrestrial analogs increase with increasing Mg content and decreasing SiO_2 content (Table 2). The liquidus temperature of the peridotitic komatiite is exceptionally high, approaching 1700°C. This temperature may not have physical meaning, as it is derived from a composition that is exceptionally enriched in Mg (43 wt % MgO, Table 2). The liquidus temperatures of the melts of Mercury surface composition are most similar to those of the Mg-adjusted magnesian basalt or basaltic komatiite.

[18] The dry viscosity, η, calculated for each model composition ranges from 0.02 to 14.2 Pa·s (Table 2). The viscosities of the various model compositions are low relative to those typical of terrestrial lavas. The viscosity of terrestrial basaltic magmas that are not enriched in Mg are at least 100 Pa·s [*Basaltic Volcanism Study Project*, 1981]. Indeed, the full range of viscosities displayed by our modeled compositions is small compared with the viscosity differences observed among typical terrestrial basaltic magmas. Among these exceptionally fluid magmas, the measured Mercury surface compositions and Indarch 1425°C melts yield the highest viscosities. The peridotitic komatiite magma has a viscosity (0.02 Pa·s) that is an order of magnitude lower than viscosities of the other modeled compositions, due to the high Mg content (and subsequent high temperature) of this magma.

3.3. Modeled X-Ray Spectra

[19] Synthetic XRS spectra for the Indarch 1425°C melt and the Mg-adjusted terrestrial analog compositions are plotted in Figure 5a along with an example XRS spectrum for the NVP (flare 2 from *Nittler et al.* [2011]). Use of this relatively low-magnitude flare spectrum to discriminate among potential analog materials is difficult because of the low signal-to-noise ratio of the observations, particularly at the higher energies. It is clear, however, that the Mg-adjusted peridotitic komatiite is a poor match to the NVP, especially in terms of Mg. Compared with the NVP spectrum, the synthetic spectra for magnesian basalt and basaltic komatiite have lower counts for Mg and Al but similar counts for Si (Figure 5a, inset). The synthetic spectrum for the Indarch melt has similar counts for Mg and Si, but lower counts for Al, than the NVP spectrum (Figure 5a, inset). A synthetic spectrum of a typical basalt (not enriched in Mg) is also plotted for comparison. This basalt is found in association with the magnesian basalt and basaltic komatiite modeled in this study [*Basaltic Volcanism Study Project*, 1981]. For this relatively low-magnitude flare, the typical basalt is not clearly differentiated in terms of Mg counts from the intermediate Mg-rich terrestrial rocks (Figure 5a, inset).

[20] Synthetic XRS spectra for the same analog compositions are shown together with an XRS spectrum (flare 5 of *Nittler et al.* [2011]) that is representative of the IcP-HCT in Figure 5b. This flare was more energetic (14.6 MK maximum solar temperature) than that which gave the spectrum in Figure 5a and therefore provided data with higher signal-to-noise ratio and the ability to evaluate additional fluorescent lines. (In order to avoid introducing errors associated with the averaging of solar spectra, a single integration's spectrum from the most energetic part of the flare was used for these comparisons.) Relative to the IcP-HCT, the peridotitic komatiite synthetic spectrum has more counts for Mg and Al and fewer counts for Si and S (Figure 5b, inset). The peridotitic komatiite also displays much fewer counts for Ca, but more counts for Ti (Figure 5b). There is an excellent match between the IcP-HCT and synthetic Mg-adjusted magnesian basalt and basaltic komatiite (Figure 5b) spectra. Although the composition of the IcP-HCT may have a slightly higher Mg content than the Mg-adjusted magnesian basalt and basaltic komatiite (Figure 5b, inset), there is complete overlap between their spectra for all other elements. It should be noted that the difference in CaO abundances between the IcP-HCT (∼6% CaO) and terrestrial analogs (∼10% CaO) is not apparent in the spectrum and thus this compositional difference is within the noise of the data. The synthetic Indarch melt spectrum has fewer counts for Mg, Al, Mn, and Fe, and more counts for Si, S, and Ca (Figure 5b). The synthetic spectrum of the typical basalt has substantially fewer counts for Mg and many more counts for Fe than the IcP-HCT spectrum and can be differentiated from the Mg-rich terrestrial rocks at this energy (Figure 5b).

4. Discussion

[21] Although the Mercury surface compositions are clearly unlike typical magma compositions in terrestrial systems, we can understand their magmatic properties and crystallization in the context of trends that are observed in mafic and ultramafic terrestrial magmas. In general, the progression from magnesian basalts through basaltic komatiites to peridotitic komatiites involves: (i) increasing Mg concentration, olivine concentration, and liquidus temperature, and (ii) decreasing Al and Si concentrations, plagioclase abundance, and viscosity. These trends are supported by the

petrology of these terrestrial rocks [*Basaltic Volcanism Study Project*, 1981]. Non-cumulate peridotitic komatiite consists of 35 to 70% olivine in a fine-grained matrix of clinopyroxene and devitrified glass. Non-cumulate basaltic komatiites contain 0 to 35% olivine in a fine-grained matrix of either clinopyroxene and devitrified glass or skeletal subcalcic clinopyroxene needles in devitrified glass. Magnesian basalts should contain little to no olivine in a plagioclase feldspar-rich groundmass, and clinopyroxene and plagioclase phenocrysts should be present in a spinifex texture, graphic intergrowths, or a subophitic texture.

[22] Measured crustal compositions for Mercury have been described as intermediate between typical basaltic compositions and more ultramafic compositions comparable to terrestrial komatiites [*Nittler et al.*, 2011]. Our work suggests that terrestrial komatiites, even when adjusted for Mg concentration, are a poor match to Mercury crustal compositions. Notably, komatiites are far more olivine-rich than the measured Mercury surface compositions, which are quartz-normative. Komatiites and Mercury compositions are also a poor match for some elements (e.g., Ca, Al) and liquidus temperature. Moreover, the mismatch in olivine abundances is generally true for basaltic komatiites, which are also olivine-rich, although these are broadly similar in composition and liquidus temperature to the Mercury compositions. Unsurprisingly, the Indarch 1425°C melts are a poor match in the derived mafic compositions, with the derived mineral compositions for measured Mercury surface compositions richer in FeO.

[23] We suggest that the Mercury surface is best described as a magnesian basalt. The Mg-adjusted magnesian basalt is a reasonably close match in mineralogy (although richer in clinopyroxene), mineral compositions, liquidus temperature, and viscosity. The Mercury compositions are best classified as norites, whereas the comparable Mg-adjusted terrestrial magnesian basalts are classified as gabbronorites.

[24] Remarkable features of the Mercury compositions and all of our candidate analogs are their exceptionally high liquidus temperatures and exceptionally low viscosities. Typical terrestrial basalts have viscosities of at least 100 Pa·s and eruptive temperatures of 1000–1200°C [*Basaltic Volcanism Study Project*, 1981]. The high liquidus temperatures and low viscosities of the modeled compositions place several constraints on the derivation and eruption style of these magmas. First, if the mantle source region of the magmas is peridotitic, either a large fraction of the source volume must have melted, or there were low degrees of partial melting of a source at high pressure. When a peridotitic source is melted, all major minerals (olivine, pyroxenes, aluminous phases) melt together. Eventually, the aluminous and calcic phases are exhausted, and mainly Mg-rich silicates (olivine, orthopyroxene) are melted so that the melt composition becomes increasingly more komatiitic as the temperature is raised farther above the solidus and higher degrees of partial melting are achieved. Increased pressure (i.e., greater depth), in contrast, stabilizes some phases (e.g., garnet) relative to olivine and orthopyroxene, so melting at high pressure preferentially melts Mg-rich silicates and thus forms a melt richer in MgO and poorer in Al_2O_3. As pressure increases, the near-solidus liquid changes from basaltic to picritic and finally to komatiitic at ~5 GPa [*Arndt*, 2008].

[25] Second, extrusion temperatures of komatiitic lavas have been estimated to be as high as 1650°C [*Green et al.*, 1975], compared with the typical eruptive temperatures of basalts at 1000–1200°C [*Basaltic Volcanism Study Project*, 1981]. Such high temperatures imply that the magma formed at greater depth and/or under higher melt fraction than those typical of the present Earth [*Basaltic Volcanism Study Project*, 1981]. The NVP and IcP-HCT both appear most similar to rocks that represent degrees of partial melting beyond those required to produce a basaltic magma.

[26] On Earth, if the upper mantle ever reached such high temperatures, much of it would have been molten [*Green et al.*, 1975]. Extensive melting of the mantle may have resulted, for instance, from impact heating early in Earth's history [*Green*, 1972]. However, high-temperature komatiitic magmas need not have required such high degrees of partial melting if their source region was sufficiently deep (150 km) [*McKenzie*, 1984; *Arndt*, 2008] or hydrated [*Arndt*, 2008]. Furthermore, since komatiites are often associated with normal basalts, it has been suggested that both magmas were formed in association with a single region of mantle upwelling, the basalts by melting at the top of the upwelling zone where magma can mix with the cooler surrounding mantle and the komatiite by melting in the deeper, hotter region of upwelling [*Campbell et al.*, 1989].

[27] Mercury's early thermal state, although poorly known, was the product of accretional heat, core-mantle differentiation, decay of short- and long-lived radioactive elements, and the loss of heat to space. No more than ~20% of the heat generated during accretion would have led to melting of nearly the entire planet [*Schubert et al.*, 1988]. By analogy with Earth and Mars, for which the Hf–W chronometer [e.g., *Kleine et al.*, 2009; *Dauphas and Pourmand*, 2011] indicates early metal–silicate separation, Mercury's core likely also formed early. The release of gravitational potential energy during core formation may have contributed an additional source of heat to increase the planet's mean temperature [e.g., *Solomon*, 1979]; core–mantle differentiation in an initially homogeneous planet would raise the mean interior temperature by as much as 700 K, but earlier metal–silicate differentiation within planetesimals [e.g., *Kleine et al.*, 2009] may have substantially limited this source of heat. A wide variety of models that consider uncertainties in the initial temperature profile of the planet, the distribution of radioactive elements, and material parameters for Mercury's interior [e.g., *Hauck et al.*, 2004; *Breuer et al.*, 2007; *Grott et al.*, 2011; *Michel et al.*, 2012; *McCubbin et al.*, 2012] indicate mantle temperatures broadly consistent with those implied by our petrologic modeling, at least during the early history of the planet. Recent models for Mercury's thermal evolution that are constrained by MESSENGER observations indicate that high-degree partial melts of a peridotitic source are possible across a wide range of mantle heat production values and initial temperatures [*Michel et al.*, 2012]. The liquidus temperatures indicated for Mercury surface material and candidate analog compositions should provide important additional constraints on the early temperature structure of Mercury.

[28] The temperatures at which magmas erupted on Mercury as well as the viscosities of the lava flows have

important implications for the morphology of volcanic features potentially observable at the surface. Lower-viscosity and higher-temperature eruptions produce thinner, more laterally extensive flow units. For example, peridotitic komatiite flows can be as thin as a few tens of centimeters over lateral extents of up to several kilometers, whereas basaltic komatiite flows tend to be at least ~1 m thick over lateral extents of hundreds of meters [*Basaltic Volcanism Study Project*, 1981]. Therefore, we would expect the flow units of the NVP and the older IcP-HCT to be thin and laterally extensive relative to most terrestrial counterparts, similar to the dimensions of a terrestrial basaltic komatiite flow. There may be modest differences between the higher-viscosity NVP lavas and the lower-viscosity (thinner, more laterally extensive) lavas in older areas on Mercury. Because of their low viscosities, these lavas would have been fluid, likely enabling them to flow around pre-existing topographic highs.

[29] The northern volcanic plains and surrounding areas display numerous features indicative of highly fluid lavas, including embayments, kipukas, lava channels, flow margins, and flow fronts [*Head et al.*, 2011]. On the basis of partially or completely buried impact craters in this region, the northern plains have been estimated to be 1 km or more in thickness and likely the product of multiple phases of emplacement with flow fronts that extend for tens to hundreds of kilometers [*Head et al.*, 2011]. These observations all support the interpretation that the northern plains were emplaced in a flood lava style. In addition, *Head et al.* [2011] documented lava-related erosion of the substrate that they suggested indicates high effusion rates, as expected for flood basalt eruptions even at the temperatures and viscosities typical of terrestrial basaltic magmas. For several wide valley systems observed in areas adjacent to the northern plains, analytical models support formation by lava erupted at high effusion rates (similar to those required to form flood basalts), first by mechanical erosion of the upper unconsolidated regolith layer and then by thermal erosion once a lower consolidated layer was encountered [*Hurwitz et al.*, 2012]. However, *Head et al.* [2011] also noted that these flows might have originated as high-temperature, low-viscosity lavas, consistent with a composition intermediate between basalts and komatiites, in which case high effusion rates need not have been required. The size-frequency distribution of impact craters on these plains shows that they are comparable in age to smooth plains elsewhere on Mercury, e.g., those interior to and surrounding the Caloris basin, indicating that this type of volcanism may have been widespread [*Head et al.*, 2011].

[30] Clearly, more work is needed to ascertain whether the flows preserved on the surface of Mercury are products of Mg-rich (and Fe-poor) lava flows that erupted at high temperatures, low viscosities, and low effusion rates, or which formed in a style more similar to that of flood basalts (with lower temperatures and higher viscosities but at high effusion rates) as proposed by *Head et al.* [2011]. To distinguish between the two types of lava flows, flow lengths and thicknesses should be examined in detail. Komatiitic and Mg-rich magmas tend to have multiple thinly bedded magma flows (on the order of 1–10 m thick) that might have erupted episodically to form a thicker stratigraphic unit [*Basaltic Volcanism Study Project*, 1981]. Flood basalts, in contrast, tend to have individual flow thicknesses of 10–50 m and accumulated thicknesses of tens of kilometers [*Basaltic Volcanism Study Project*, 1981]. Flow lengths and fluid flow features should be documented [e.g., *Head et al.*, 2011] for multiple examples on Mercury from high-resolution orbital images, and flow thickness should be estimated from imaging and altimetry. MESSENGER's imaging system and laser altimeter [*Solomon et al.*, 2001] have sufficient resolution to provide the details needed to evaluate the characteristics of major lava flows on Mercury. In addition, analytical modeling of lava erosion [e.g., *Hurwitz et al.*, 2012] should be carried out for magmas having the compositions indicated by this study to determine which provide the best explanation for the lava channels observed on Mercury.

5. Conclusions

[31] This work leads to several important conclusions.

[32] 1. The surface composition of Mercury is most similar to that of a terrestrial magnesian basalt (with lower FeO) and consists mainly of Mg-rich orthopyroxene and plagioclase. This result is consistent with the finding that the XRS-derived surface compositions are intermediate between those of basalts and komatiites [*Nittler et al.*, 2011].

[33] 2. Surface material on Mercury is Mg-rich, so lavas would have erupted at high temperatures and would have displayed low viscosities. The viscosities would have been on the order of that for a magnesian basalt, but as much as two orders of magnitude lower than for a typical basaltic magma on Earth.

[34] 3. Producing melts of these compositions required high temperatures (≥1500°C) in the mantle source regions of these magmas.

[35] 4. The inferred low-viscosity lavas would have erupted as thin, laterally extensive flows (depending upon their effusion rate) and would be expected to have formed surficial flow features, as have been identified in Mercury's northern plains and adjacent areas [*Head et al.*, 2011].

[36] **Acknowledgments.** We thank the MESSENGER science and engineering teams for their development and execution of the MESSENGER mission and for their acquisition and analysis of mission data, which made this work possible. We also thank Francis McCubbin and an anonymous reviewer for insightful reviews of this manuscript. This work is supported by a MESSENGER Participating Scientist Program grant to T.J.M. The MESSENGER project is supported by the NASA Discovery Program under contracts NASW-00002 to the Carnegie Institution of Washington and NAS5–97271 to The Johns Hopkins University Applied Physics Laboratory.

References

Arndt, N. T. (2008), *Komatiite*, 467 pp., Cambridge Univ. Press, Cambridge, U. K., doi:10.1017/CBO9780511535550.

Asimov, P. D., and M. S. Ghiorso (1998), Algorithmic modifications extending MELTS to calculate subsolidus phase relations, *Am. Mineral.*, *83*, 1127–1131.

Basaltic Volcanism Study Project (1981), *Basaltic Volcanism on the Terrestrial Planets*, 1286 pp., Pergamon, New York.

Blewett, D. T., B. R. Hawke, and P. G. Lucey (2002), Lunar pure anorthosite as a spectral analog for Mercury, *Meteorit. Planet. Sci.*, *37*, 1245–1254, doi:10.1111/j.1945-5100.2002.tb00893.x.

Blewett, D. T., M. S. Robinson, B. W. Denevi, J. J. Gillis-Davis, J. W. Head, S. C. Solomon, G. M. Holsclaw, and W. E. McClintock (2009), Multispectral images of Mercury from the first MESSENGER flyby: Analysis of global and regional color trends, *Earth Planet. Sci. Lett.*, *285*, 272–282, doi:10.1016/j.epsl.2009.02.021.

Breuer, D., S. A. Hauck II, M. Buske, M. Pauer, and T. Spohn (2007), Interior evolution of Mercury, *Space Sci. Rev.*, *132*, 229–260, doi:10.1007/s11214-007-9228-9.

Burbine, T. H., T. J. McCoy, L. R. Nittler, G. K. Benedix, E. A. Cloutis, and T. L. Dickinson (2002), Spectra of extremely reduced assemblages: Implications for Mercury, *Meteorit. Planet. Sci.*, *37*, 1233–1244, doi:10.1111/j.1945-5100.2002.tb00892.x.

Campbell, I. H., R. W. Griffiths, and R. I. Hill (1989), Melting in an Archaean mantle plume: Heads it's basalts, tails it's komatiites, *Nature*, *339*, 697–699, doi:10.1038/339697a0.

Chapman, C. R. (1988), Mercury: Introduction to an end-member planet, in *Mercury*, edited by F. Vilas, C. R. Chapman, and M. S. Matthews, pp. 1–23, Univ. of Ariz. Press, Tucson.

Clark, P. E., and J. I. Trombka (1997), Remote X-ray spectrometry for NEAR and future missions: Modeling and analyzing X-ray production from source to surface, *J. Geophys. Res.*, *102*, 16,361–16,384, doi:10.1029/97JE01086.

Dauphas, N., and A. Pourmand (2011), Hf-W-Th evidence for rapid growth of Mars and its status as a planetary embryo, *Nature*, *473*, 489–492, doi:10.1038/nature10077.

Denevi, B. W., and M. S. Robinson (2008), Mercury's albedo from Mariner 10: Implications for the presence of ferrous iron, *Icarus*, *197*, 239–246, doi:10.1016/j.icarus.2008.04.021.

Dere, K. P., E. Landi, H. E. Mason, B. C. Monsignori Fossi, and P. R. Young (1997), CHIANTI–An atomic database for emission lines, *Astron. Astrophys. Suppl. Ser.*, *125*, 149–173, doi:10.1051/aas:1997368.

Evans, L. G., et al. (2012), Major element abundances on the surface of Mercury: Results from the MESSENGER Gamma-Ray Spectrometer, *J. Geophys. Res.*, *117*, E00L07, doi:10.1029/2012JE004178.

Ghiorso, M. S., and R. O. Sack (1995), Chemical mass transfer in magmatic processes. IV. A revised and internally consistent thermodynamic model for the interpolation and extrapolation of liquid-solid equilibria in magmatic systems at elevated temperatures and pressures, *Contrib. Mineral. Petrol.*, *119*, 197–212, doi:10.1007/BF00307281.

Green, D. H. (1972), Archaean greenstone belts may include terrestrial equivalents of lunar maria?, *Earth Planet. Sci. Lett.*, *15*, 263–270, doi:10.1016/0012-821X(72)90172-0.

Green, D. H., I. A. Nicholls, M. Viljoen, and R. Viljoen (1975), Experimental determination of the existence of peridotite liquids in earliest Archaean magmatism, *Geology*, *3*, 11–14, doi:10.1130/0091-7613(1975)3<11:EDOTEO>2.0.CO;2.

Grott, M. D., D. Breuer, and M. Laneuville (2011), Thermo-chemical evolution and global contraction of Mercury, *Earth Planet. Sci. Lett.*, *307*, 135–146, doi:10.1016/j.epsl.2011.04.040.

Hauck, S. A., II, A. J. Dombard, R. J. Phillips, and S. C. Solomon (2004), Internal and tectonic evolution of Mercury, *Earth Planet. Sci. Lett.*, *222*, 713–728, doi:10.1016/j.epsl.2004.03.037.

Head, J. W., et al. (2011), Flood volcanism in the northern high latitudes of Mercury revealed by MESSENGER, *Science*, *333*, 1853–1856, doi:10.1126/science.1211997.

Hurwitz, D. M., J. W. Head, P. K. Byrne, Z. Xiao, S. C. Solomon, M. T. Zuber, D. E. Smith, and G. A. Neumann (2012), Investigating the origin of candidate lava channels on Mercury observed in MESSENGER data: Theory and observations, *J. Geophys. Res.*, doi:10.1029/2012JE004103, in press.

Kleine, T., M. Touboul, B. Bourdo, F. Nimmo, K. Mezger, H. Palme, S. B. Jacobsen, Q.-Z. Yin, and A. N. Halliday (2009), Hf–W chronology of the accretion and early evolution of asteroids and terrestrial planets, *Geochim. Cosmochim. Acta*, *73*, 5150–5188, doi:10.1016/j.gca.2008.11.047.

Landi, E., G. Del Zanna, P. R. Young, K. P. Dere, H. E. Mason, and M. Landini (2006), CHIANTI–An atomic database for emission lines. VII. New data for X-rays and other improvements, *Astrophys. J. Suppl. Ser.*, *162*, 261–280, doi:10.1086/498148.

Lodders, K., and B. Fegley (1998), *The Planetary Scientist's Companion*, 371 pp., Oxford Univ. Press, New York.

Malavergne, V., M. J. Toplis, S. Berthet, and J. Jones (2010), Highly reducing conditions during core formation on Mercury: Implications for internal structure and origin of the magnetic field, *Icarus*, *206*, 199–209, doi:10.1016/j.icarus.2009.09.001.

McClintock, W. E., et al. (2008), Spectroscopic observations of Mercury's surface reflectance during MESSENGER's first Mercury flyby, *Science*, *321*, 62–65, doi:10.1126/science.1159933.

McCoy, T. J., T. L. Dickinson, and G. E. Lofgren (1999), Partial melting of the Indarch (EH4) meteorite: A textural, chemical, and phase relations view of melting and melt migration, *Meteorit. Planet. Sci.*, *34*, 735–746, doi:10.1111/j.1945-5100.1999.tb01386.x.

McCubbin, F. M., M. A. Riner, K. E. Vander Kaaden, and L. K. Burkemper (2012), Is Mercury a volatile-rich planet?, *Geophys. Res. Lett.*, *39*, L09202, doi:10.1029/2012GL051711.

McKenzie, D. (1984), The generation and compaction of partially molten rock, *J. Petrol.*, *25*, 713–765.

Michel, N. C., S. A. Hauck II, S. C. Solomon, R. J. Phillips, J. H. Roberts, and M. T. Zuber (2012), Implications of MESSENGER observations for mantle convection on Mercury, *Lunar Planet. Sci.*, *XLIII*, Abstract 1671.

Morgan, J. W., and E. Anders (1980), Chemical composition of Earth, Venus, and Mercury, *Proc. Natl. Acad. Sci. U. S. A.*, *77*, 6973–6977, doi:10.1073/pnas.77.12.6973.

Nittler, L. R., et al. (2001), X-ray fluorescence measurements of the surface composition of asteroid 433 Eros, *Meteorit. Planet. Sci.*, *36*, 1673–1695, doi:10.1111/j.1945-5100.2001.tb01856.x.

Nittler, L. R., et al. (2011), The major-element composition of Mercury's surface from MESSENGER X-ray spectrometry, *Science*, *333*, 1847–1850, doi:10.1126/science.1211567.

Papike, J. J., G. Ryder, and C. K. Shearer (1998), Lunar samples, in *Planetary Materials*, edited by J. J. Papike, pp. 5.1–5.234, Mineral. Soc. of Am., Washington, D. C.

Peplowski, P. N., et al. (2011), Radioactive elements on Mercury's surface from MESSENGER: Implications for the planet's formation and evolution, *Science*, *333*, 1850–1852, doi:10.1126/science.1211576.

Riner, M. A., F. M. McCubbin, P. G. Lucey, G. J. Talyor, and J. J. Gillis-Davis (2010), Mercury surface composition: Integrating petrologic modeling and remote sensing data to place constraints on FeO abundance, *Icarus*, *209*, 301–313, doi:10.1016/j.icarus.2010.05.018.

Robinson, M. S., and G. J. Taylor (2001), Ferrous oxide in Mercury's crust and mantle, *Meteorit. Planet. Sci.*, *36*, 841–847, doi:10.1111/j.1945-5100.2001.tb01921.x.

Schlemm, C. E., II, et al. (2007), The X-Ray Spectrometer on the MESSENGER spacecraft, *Space Sci. Rev.*, *131*, 393–415, doi:10.1007/s11214-007-9248-5.

Schubert, G., M. N. Ross, D. J. Stevenson, and T. Spohn (1988), Mercury's thermal history and the generation of its magnetic field, in *Mercury*, edited by F. Vilas, C. R. Chapman, and M. S. Matthews, pp. 429–460, Univ. of Ariz. Press, Tucson.

Shaw, H. R. (1972), Viscosities of magmatic silicate liquids; an empirical method of prediction, *Am. J. Sci.*, *272*, 870–893, doi:10.2475/ajs.272.9.870.

Slater, V. P., C. K. Thompson, J. Nettles, K. Milam, K. R. Stockstill, J. Cahill, M. Anand, and L. A. Taylor (2003), An evaluation of the igneous crystallization programs–MELTS, MAGPOX, and COMAGMAT, Part II: Importance of magmatic fO_2, *Lunar Planet. Sci.*, *XXXIV*, Abstract 1896.

Solomon, S. C. (1979), Formation, history and energetics of cores in the terrestrial planets, *Phys. Earth Planet. Inter.*, *19*, 168–182, doi:10.1016/0031-9201(79)90081-5.

Solomon, S. C., et al. (2001), The MESSENGER mission to Mercury: Scientific objectives and implementation, *Planet. Space Sci.*, *49*, 1445–1465, doi:10.1016/S0032-0633(01)00085-X.

Sprague, A. L., K. L. Donaldson Hanna, R. W. H. Kozlowski, J. Helbert, A. Maturilli, J. B. Warell, and J. L. Hora (2009), Spectral emissivity measurements of Mercury's surface indicate Mg- and Ca-rich mineralogy, K-spar, Na-rich plagioclase, rutile, with possible perovskite, and garnet, *Planet. Space Sci.*, *57*, 364–383, doi:10.1016/j.pss.2009.01.006.

Spudis, P. D., and J. E. Guest (1988), Stratigraphy and geologic history of Mercury, in *Mercury*, edited by F. Vilas, C. R. Chapman, and M. S. Matthews, pp. 374–400, Univ. of Ariz. Press, Tucson.

Taylor, G. J., and E. R. D. Scott (2003), Mercury, in *Treatise on Geochemistry*, vol. 1, *Meteorites, Comets, and Planets*, edited by A. M. Davis, pp. 477–485, Elsevier, Oxford, U. K.

Thompson, C. K., V. P. Slater, K. R. Stockstill, M. Anand, J. Nettles, K. Milam, J. Cahill, and L. A. Taylor (2003), An evaluation of the igneous crystallization programs–MELTS, MAGPOX and COMAGMAT, Part I: Does one size fit all?, *Lunar Planet. Sci.*, *XXXIV*, Abstract 1681.

Vilas, F. (1988), Surface composition of Mercury from reflectance spectrophotometry, in *Mercury*, edited by F. Vilas, C. R. Chapman, and M. S. Matthews, pp. 59–76, Univ. of Ariz. Press, Tucson.

Weider, S. Z., L. R. Nittler, R. D. Starr, T. J. McCoy, K. R. Stockstill-Cahill, P. K. Byrne, B. W. Denevi, J. W. Head, and S. C. Solomon (2012), Chemical heterogeneity on Mercury's surface revealed by the MESSENGER X-Ray Spectrometer, *J. Geophys. Res.*, *117*, E00L05, doi:10.1029/2012JE004153.

Zolotov, M. Y. (2011), On the chemistry of mantle and magmatic volatiles on Mercury, *Icarus*, *212*, 24–41, doi:10.1016/j.icarus.2010.12.014.